



# Microstructural Feature and Evolution of Rapidly Solidified Ni<sub>3</sub>Al-Based Superalloys

Ye-Fan Li<sup>1</sup> · Chong Li<sup>1</sup> · Jing Wu<sup>1</sup> · Hui-Jun Li<sup>1</sup> · Yong-Chang Liu<sup>1</sup> · Hai-Peng Wang<sup>2</sup>

Received: 23 July 2018 / Revised: 30 August 2018 / Published online: 1 November 2018  
© The Chinese Society for Metals and Springer-Verlag GmbH Germany, part of Springer Nature 2018

## Abstract

The Ni<sub>3</sub>Al-based superalloy was rapidly solidified in the form of droplets with varying diameters. The cooling rate ( $R_c$ ) is a function of diameter ( $D$ ) of droplet. With the decrease in droplet sizes (increase in the cooling rates), the volume fraction of  $\gamma' + \gamma$  eutectic structure increases from 21.31 ( $D = 1400 \mu\text{m}$ ,  $R_c = 3.6 \times 10^2 \text{ K s}^{-1}$ ) to 36.31% ( $D = 270 \mu\text{m}$ ,  $R_c = 2.3 \times 10^3 \text{ K s}^{-1}$ ). Moreover, unimodal size distribution of nano- $\gamma'$  exists in the droplets instead of bimodal dual-size distributions of  $\gamma'$  precipitates that are normal in as-cast alloys.

**Keywords** Ni<sub>3</sub>Al-based superalloy · Microstructure · Rapid solidification ·  $\gamma'$  precipitate

## 1 Introduction

Ni-based superalloys have been characterized as excellent comprehensive properties (high temperature strength, creep resistances, and good high-temperature oxidation resistance) [1–3]. These alloys have been widely used in various aerospace turbine blades, heat-treating fixtures for carburizing and oxidizing environments, tube hangers for high-temperature processing furnaces, and so on [4–8]. In order to further improve high-temperature mechanical properties [9] and decrease the density, Ni<sub>3</sub>Al-based superalloys were developed based on Ni-based superalloys in the 1980s, which had the most important characteristic of high Al content [10–12].

Solidification conditions [13, 14] have a great influence on the as-cast microstructures of Ni-/Ni<sub>3</sub>Al-based superalloys, such as the temperature gradient and

withdrawal/cooling rate. In particular, the withdrawal rate (for single crystal) or cooling rate (for polycrystalline alloy) is a critical parameter, which plays an important role in determining the microstructural transition and phase development [15–19].

Comprehensive understanding for development of microstructure at a wide range of withdrawal/cooling rates is necessary and quantitative. Analysis of microstructure evolution can support an experimental proof for establishing casting and solid solution + aging process. For single-crystal Ni-/Ni<sub>3</sub>Al-based superalloys, a lot of studies [15–17] have reported the relationship between microstructural evolution and withdrawal rates. These studies demonstrate a typical behavior that the morphology and size distribution of  $\gamma'$  precipitates are closely associated with withdrawal rates during directional solidification [16]. However, the microstructural evolution of polycrystalline Ni<sub>3</sub>Al-based superalloys in rapidly solidified conditions (a wide range of cooling rates and drop tube techniques here) has not been explained clearly in the previous work.

Rapid solidification under high undercooling conditions can be accomplished by several ways, such as glass-fluxing method, rapid quenching, emulsification, levitation processing, and drop tube techniques. Compared with the other methods, the drop tube technique is characterized by rapid cooling [20]. Drop tube is a preferable choice to study non-equilibrium solidification process. In this work, a polycrystalline Ni<sub>3</sub>Al-based alloy was used as the matrix. The purpose of this work is to provide a deep insight into

Available online at <http://link.springer.com/journal/40195>.

✉ Chong Li  
lichongme@tju.edu.cn

✉ Yong-Chang Liu  
licmtju@163.com

<sup>1</sup> State Key Lab of Hydraulic Engineering Simulation and Safety, School of Materials Science and Engineering, Tianjin University, Tianjin 300354, China

<sup>2</sup> Department of Applied Physics, School of Science, Northwestern Polytechnical University, Xi'an 710129, China

the microstructural feature and evolution of rapidly solidified polycrystalline Ni<sub>3</sub>Al-based superalloys (under free-fall condition).

## 2 Experimental

The Ni<sub>3</sub>Al-based superalloy used in this work was produced by vacuum induction melting (VIM) and electroslag remelting (ESR) techniques; the chemical composition of the alloy is listed in Table 1, and the droplet samples were obtained by drop tube technique. The drop tube was evacuated to  $2 \times 10^{-4}$  Pa and backfilled with argon gas to  $1 \times 10^5$  Pa. Superheating above the liquidus temperature was accomplished by induction heating.

After that, the bulk sample was dispersed into small droplets by high-pressure Ar jetting gas. The small droplets with different diameters fell down freely and were rapidly solidified during free fall in drop tube. The finally solidified particles were mounted in epoxy, polished, and etched with a mixture solution of 10 ml H<sub>2</sub>O + 30 ml HCl + 5 g Cr<sub>2</sub>O<sub>3</sub>. The microstructures were mainly analyzed by optical microscopy (OM) and S4800 scanning electron microscopy (SEM). Transmission electron microscopy (TEM) analysis was performed using an FEI Tecnai G2 F20 transmission electron microscope, operated at 200 keV. The foils for TEM observation were prepared by grinding using progressively finer SiC paper to a thickness of 40 μm. The final thinning was performed by the method of ion-beam thinning. A differential scanning calorimeter (DSC) STA449C test was performed to study the different solidification sequences of as-cast alloy and droplet samples. As-cast sample and droplet samples were completely melted by heating to 1500 °C and then cooled to 600 °C at a constant rate of 10 °C/min in an argon atmosphere.

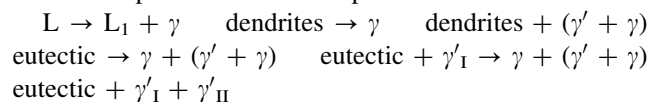
## 3 Results and Discussion

### 3.1 Microstructures of the as-cast Ni<sub>3</sub>Al-Based Superalloy

The SEM images of as-cast Ni<sub>3</sub>Al-based superalloys are shown in Fig. 1. It can be seen that the microstructure consists of primary dendrites and interdendritic regions ( $\gamma' + \gamma$  eutectic) (Fig. 1a). The volume fraction of  $\gamma' + \gamma$  eutectic is measured to be about 19.37%. As illustrated in the enlarged morphology of dendrite (Fig. 1b), a lot of

cuboidal  $\gamma'$  precipitates ( $\gamma'_{\text{I}}$ ) are distributed uniformly with the mean size of 0.5 μm. Moreover, adjacent cuboidal  $\gamma'$  precipitates are separated by  $\gamma$ -phase channels, in which nanometric  $\gamma'$  particles ( $\gamma'_{\text{II}}$ ) are homogeneously formed (Fig. 1b). As shown in Fig. 1c, it can be seen that the size of  $\gamma'_{\text{II}}$  particles is about 10–30 nm.

According to Ni–Al phase diagram [21] and the previous research results [22], the solidification path of the as-cast Ni<sub>3</sub>Al-based superalloy can be indicated as sequence (1). During cooling process, the primary dendrites ( $\gamma$  solid-solution phase) firstly solidify from liquid melt. And then, the residual liquid transforms into interdendritic phases through  $\gamma' + \gamma$  eutectic. During the subsequent cooling process of solid phase, cuboidal  $\gamma'$  particles precipitate from dendritic  $\gamma$  solid solution (marked as  $\gamma'_{\text{I}}$ ). The initial  $\gamma$  phase is divided into narrow channels located among cuboidal  $\gamma'$  phases. At the latest cooling stage, quasi-spherical  $\gamma'$  phases (marked as  $\gamma'_{\text{II}}$ ) form in the  $\gamma$  channels. The above processes can be explained as:



The results of DSC test carried out for as-cast Ni<sub>3</sub>Al-based superalloy are shown in Fig. 2. The exothermic peak A (Fig. 2a) can be ascribed to the formation of primary dendrites ( $\gamma$  solid-solution phase). The peak of B is corresponding to the process of binary eutectic reaction ( $\gamma' + \gamma$  eutectic). In order to clearly explain the stage of  $\gamma'$  precipitation from  $\gamma$  solid solution, the area C (Fig. 2a) is enlarged and shown in Fig. 2b, from which it can be seen that there are two exothermic peaks. The exothermic peaks around 1130 and 1075 °C can be explained as the peak temperatures for the precipitation of  $\gamma'_{\text{I}}$  and  $\gamma'_{\text{II}}$  from dendritic  $\gamma$ , respectively.

### 3.2 Calculated Relationship Between Diameter and Cooling Rate of Droplets

Droplets with different diameters (cooling rates) were obtained through drop tube technique. A bulk sample of alloy melt was dispersed into a lot of small droplets during the experiment, and then, these droplets fell freely in a drop tube full of Ar gas environment. It is quite difficult to directly measure the cooling rates of droplets within the short period of falling time. In the drop tube, the cooling rate of droplets depends on their sizes during free fall in drop tube full of Ar. For the calculation of cooling rate ( $R_c$ ), as a function of diameter ( $D$ ) of droplet, according to

**Table 1** Chemical composition of Ni<sub>3</sub>Al-based superalloy (wt%)

Al	Cr	Mo	W	C	Si	Hf	B	Mn	Ti	Fe	Ni
7.6–8.5	7.4–8.2	3.5–5.5	1.5–2.5	0.06–0.2	< 0.5	0.3–0.9	< 0.05	< 0.5	0.6–1.2	< 2	Bal.

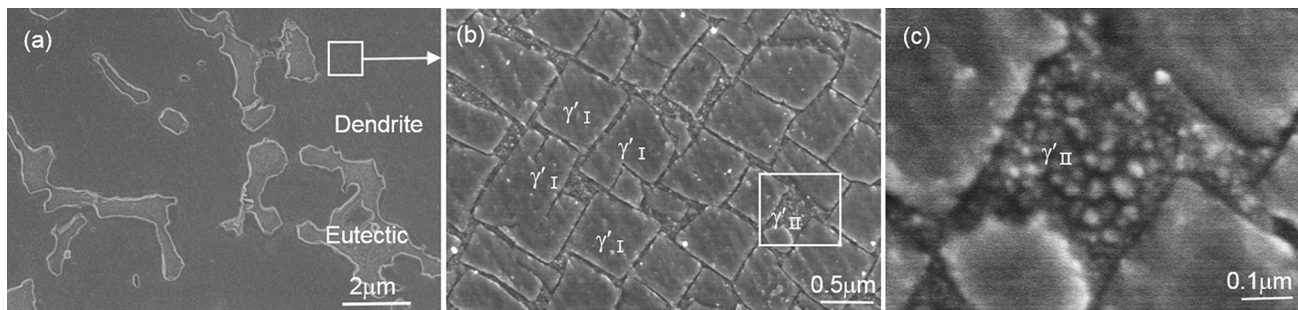


Fig. 1 a Microstructure of as-cast Ni<sub>3</sub>Al-based superalloy, b morphology of γ' particles (in primary dendrites), c enlarged image of γ' II particles

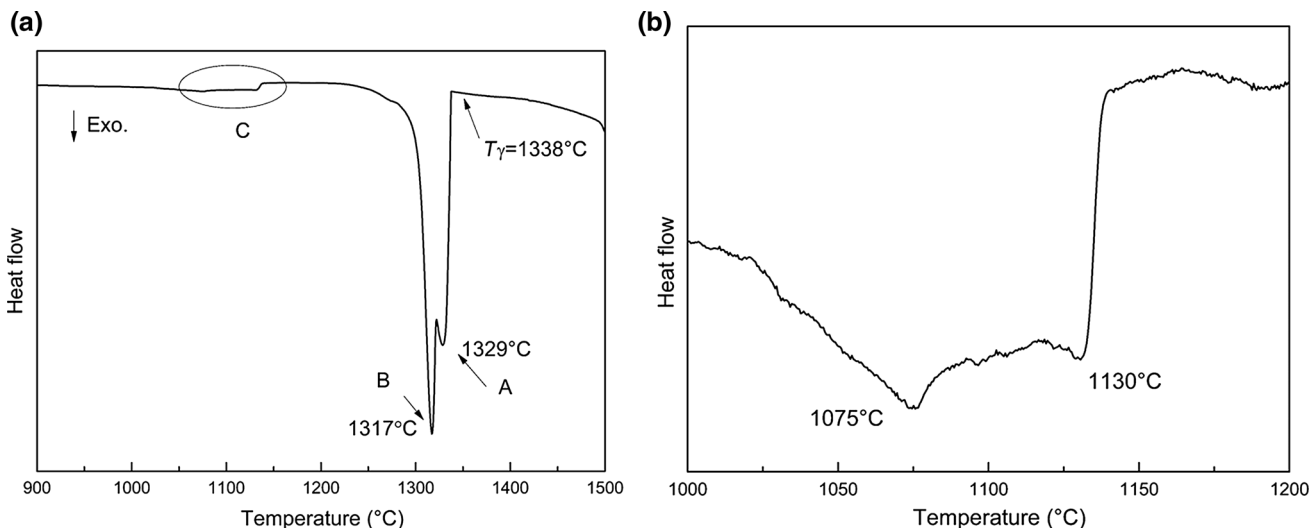


Fig. 2 a DSC result of as-cast Ni<sub>3</sub>Al-based superalloy, b enlarged area C in Fig. 2a

the Newtonian model [23], the heat transfer can be described by Eq. (1):

$$R_c = \frac{6}{\rho_L C_{PL} D} [\epsilon_h k_{SB} (T^4 - T_0^4) + h(T - T_0)], \quad (1)$$

where  $\rho_L$  is the mass density of the melt,  $C_{PL}$  is the specific heat of the liquid phase (444 J/(kg K)),  $\epsilon_h$  is the coefficient of thermal radiation on the surface of the alloy (0.35),  $h$  is the convective heat transfer coefficient,  $k_{SB}$  is the Stefan–Boltzmann constant ( $5.67 \times 10^{-8}$ ),  $T$  is the liquidus temperature, and  $T_0$  is the temperature of environmental gas.

In the case of droplets motioning in gas, the convective heat transfer coefficient ( $h$ ) is confirmed by the rule of heat transfer equation given in Eq. (2):

$$Nu = 2 + 0.6Pr^{\frac{1}{3}}Re^{\frac{1}{2}}. \quad (2)$$

The Nusselt number (Nu) [24] is  $hD/\lambda_0$ , the Reynolds number (Re) is  $\rho_0 V_r D/\eta_0$ , and the Prandtl number (Pr) is  $\eta_0 C_{P0}/\lambda_0$ .  $V_r$  is the kinematic velocity of droplet moving in the gas. Meanwhile,  $\rho_0$  (0.266 kg/m<sup>3</sup>),  $\eta_0$  ( $7.6 \times 10^{-3}$ ),  $C_{P0}$  (520 J/(kg K)), and  $\lambda_0$  ( $6.26 \times 10^{-2}$ ) are gas constants.

Based on Eqs. 1 and 2, the calculated results of relationship between cooling rate ( $R_c$ ) and diameter ( $D$ ) of droplet are presented in Fig. 3. It indicates that the cooling rate increases with decreasing droplet diameter. The cooling rate of the smallest alloy droplet with a diameter of

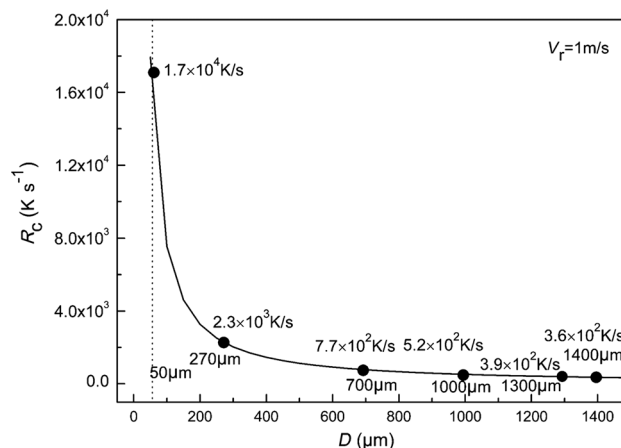
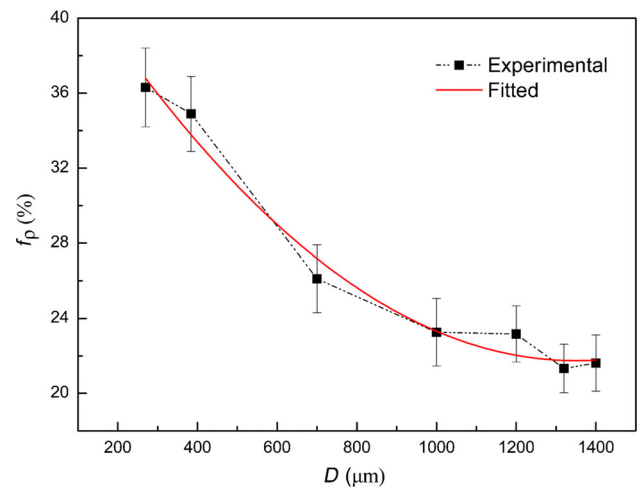


Fig. 3 Calculated relationship between diameter ( $D$ ) and cooling rate ( $R_c$ )

50  $\mu\text{m}$  can achieve  $1.7 \times 10^4 \text{ K s}^{-1}$ . In contrast, the cooling rate is reduced to only  $3.6 \times 10^2 \text{ K s}^{-1}$ , while the droplet diameter increases to 1400  $\mu\text{m}$ .

### 3.3 Relationship Between Cooling Rate and Microstructure of Droplets

In order to reveal the evolution of eutectic structure with the change of cooling rates, the eutectic structures of droplets with different diameters (cooling rates) were extracted by ImageJ software. Figure 4 shows the images of extracted eutectic structures of droplets with typical diameters ( $D = 1300 \mu\text{m}$ ,  $R_c = 3.9 \times 10^2 \text{ K s}^{-1}$ ;  $D = 1000 \mu\text{m}$ ,  $R_c = 5.2 \times 10^2 \text{ K s}^{-1}$ ;  $D = 700 \mu\text{m}$ ,  $R_c = 7.7 \times 10^2 \text{ K s}^{-1}$ ;  $D = 270 \mu\text{m}$ ,  $R_c = 2.3 \times 10^3 \text{ K s}^{-1}$ ). It is noticed that the volume fraction of eutectic structure obviously increases with the increase in cooling rates. Ten randomly selected zones for each droplet were calculated to get average characteristic value for the volume fraction of eutectic structure. The corresponding relationship between volume fraction of eutectic structure ( $f_p$ ) and droplet diameter ( $D$ ) is presented in Fig. 5. The volume fraction of  $\gamma' + \gamma$  eutectic ( $f_p$ ) continuously increases with decreasing droplet diameter ( $D$ ). As mentioned above, the  $\gamma' + \gamma$  eutectic is generated from residual liquid after the finishing of precipitation of primary dendrites ( $\gamma$  solid solution). The droplets were cooled (non-



**Fig. 5** Average volume fraction of eutectic phase versus droplet diameter

equilibrium solidification) so fast that there was limited time for the precipitation of primary dendrites from the liquid. Therefore, the cooling rate increases with the decrease in droplet diameter, which leads to the reduction of the formation of primary dendrites. The increasing remanent liquid completely solidified into eutectic structures, resulting in the increase in volume fraction of  $\gamma' + \gamma$  eutectic (Fig. 4). As the cooling rate increases from  $3.6 \times 10^2 \text{ K s}^{-1}$

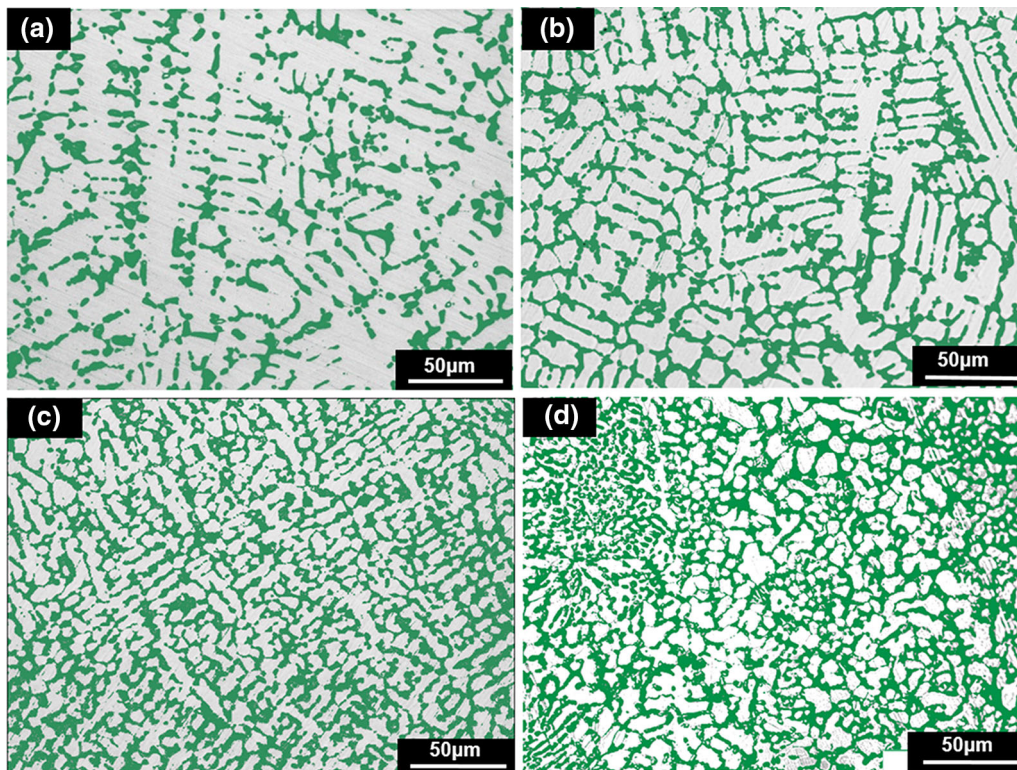


**Fig. 4** Images of eutectic structures extracted by ImageJ software: **a**  $D = 1300 \mu\text{m}$  ( $R_c = 3.9 \times 10^2 \text{ K s}^{-1}$ ), **b**  $D = 1000 \mu\text{m}$  ( $R_c = 5.2 \times 10^2 \text{ K s}^{-1}$ ), **c**  $D = 700 \mu\text{m}$  ( $R_c = 7.7 \times 10^2 \text{ K s}^{-1}$ ), **d**  $D = 270 \mu\text{m}$  ( $R_c = 2.3 \times 10^3 \text{ K s}^{-1}$ )

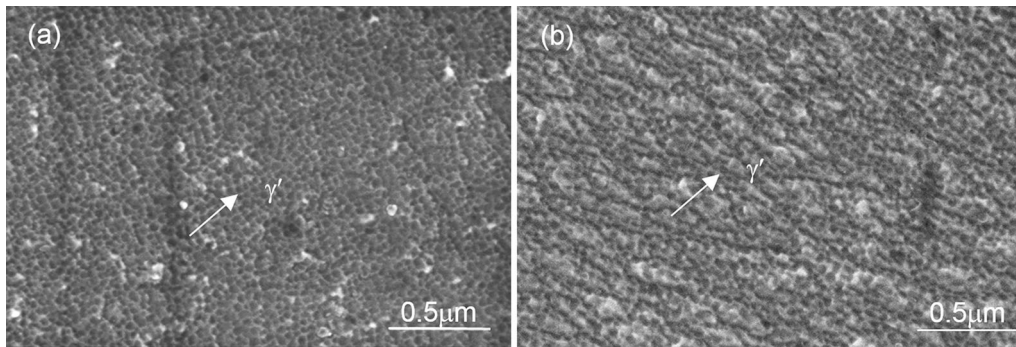


**Fig. 6** Morphology of  $\gamma'$  particles (precipitating from dendritic  $\gamma$  solid solution) of the droplet sample with different diameters: **a** 1000  $\mu\text{m}$  ( $R_c = 5.2 \times 10^2 \text{ K s}^{-1}$ ), **b** 700  $\mu\text{m}$  ( $R_c = 7.7 \times 10^2 \text{ K s}^{-1}$ )

( $D = 1400 \mu\text{m}$ ) to  $2.3 \times 10^3 \text{ K s}^{-1}$  ( $D = 270 \mu\text{m}$ ), the volume fraction of  $\gamma' + \gamma$  eutectic increases from 21.33% to 36.31% (Fig. 5), compared to 19.37% in as-cast sample.

Moreover, the morphology and size of  $\gamma'$  particles (precipitating from dendritic  $\gamma$  solid solution) are also changed (Fig. 6), compared to as-cast alloy (Fig. 1b). In as-cast  $\text{Ni}_3\text{Al}$ -based superalloy (Fig. 1b), bimodal dual-size distributions of  $\gamma'$  precipitates can be observed: large cuboidal  $\gamma'_{\text{I}}$  precipitates and nano-quasi-spherical  $\gamma'_{\text{II}}$  precipitates within the  $\gamma$  phase (Fig. 1). However, the unimodal distribution of nanoscale  $\gamma'$  precipitates exists in the microstructure of rapidly solidified droplets (Fig. 6). Moreover, with the cooling rate increasing from  $5.2 \times 10^2 \text{ K s}^{-1}$  ( $D = 1000 \mu\text{m}$ ) to  $2.3 \times 10^3 \text{ K s}^{-1}$  ( $D = 700 \mu\text{m}$ ), the size of nano- $\gamma'$  precipitates has a decreasing tendency (as shown in Fig. 6). TEM image and corresponding selected area electron diffraction (SAED) pattern of the droplet sample ( $D = 1000 \mu\text{m}$ ,  $R_c = 5.2 \times 10^2 \text{ K s}^{-1}$ ) are shown in Fig. 7. It can be seen

that the  $\gamma'$  phase with size about 30–50 nm presents unimodal distribution in the  $\gamma$  phase.

$\gamma'$  precipitation occurs in three stages: nucleation, growth, and coarsening [25]. In the as-cast alloy, the nucleation rate is sluggish and most of the transformation is controlled initially by growth and subsequently by coarsening. There is enough time for diffusional transport of atoms with slow cooling rate. Continued growth of the  $\gamma'$  precipitates evolves the system into a state close to equilibrium, after which further evolution is driven by the minimization of the total precipitate surface area. Therefore, large  $\gamma'$  precipitates ( $\gamma'_{\text{I}}$ ) are promoted. Moreover, on further cooling, the extension of the diffusion fields shrinks due to reduced diffusional transport. Corridors between the precipitates open, which are essentially unaffected by the continued growth of the existing precipitates [25]. In these corridors, supersaturation increases rapidly again until a second nucleation burst occurs. As a result of this interaction, the bimodal dual sizes of  $\gamma'$  precipitates are

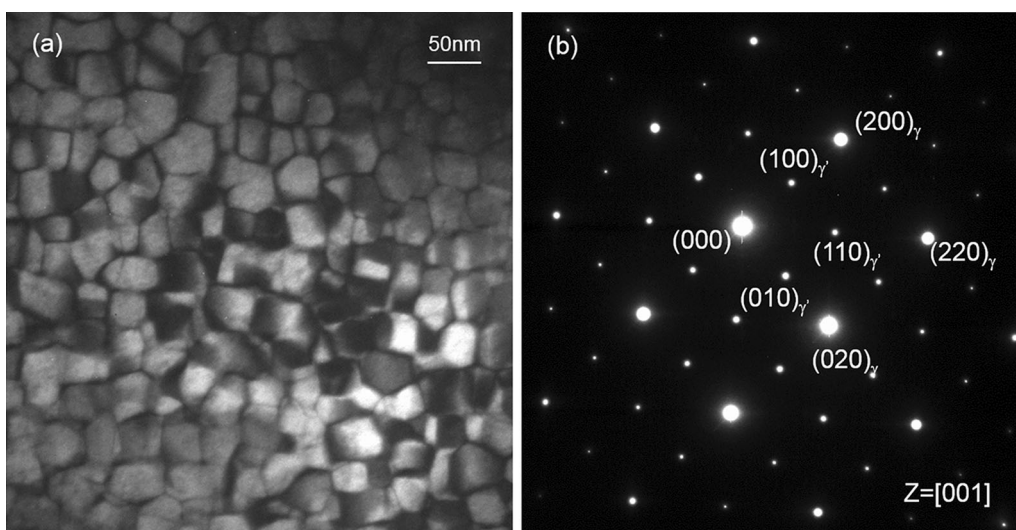


**Fig. 7** **a** TEM micrograph of  $\gamma'$  particles in the droplet sample with diameter of 1000  $\mu\text{m}$  ( $R_c = 5.2 \times 10^2 \text{ K s}^{-1}$ ), **b** corresponding SAED pattern showing the  $\gamma$  matrix,  $\gamma'$  precipitates of the alloys.  $Z = [001]$

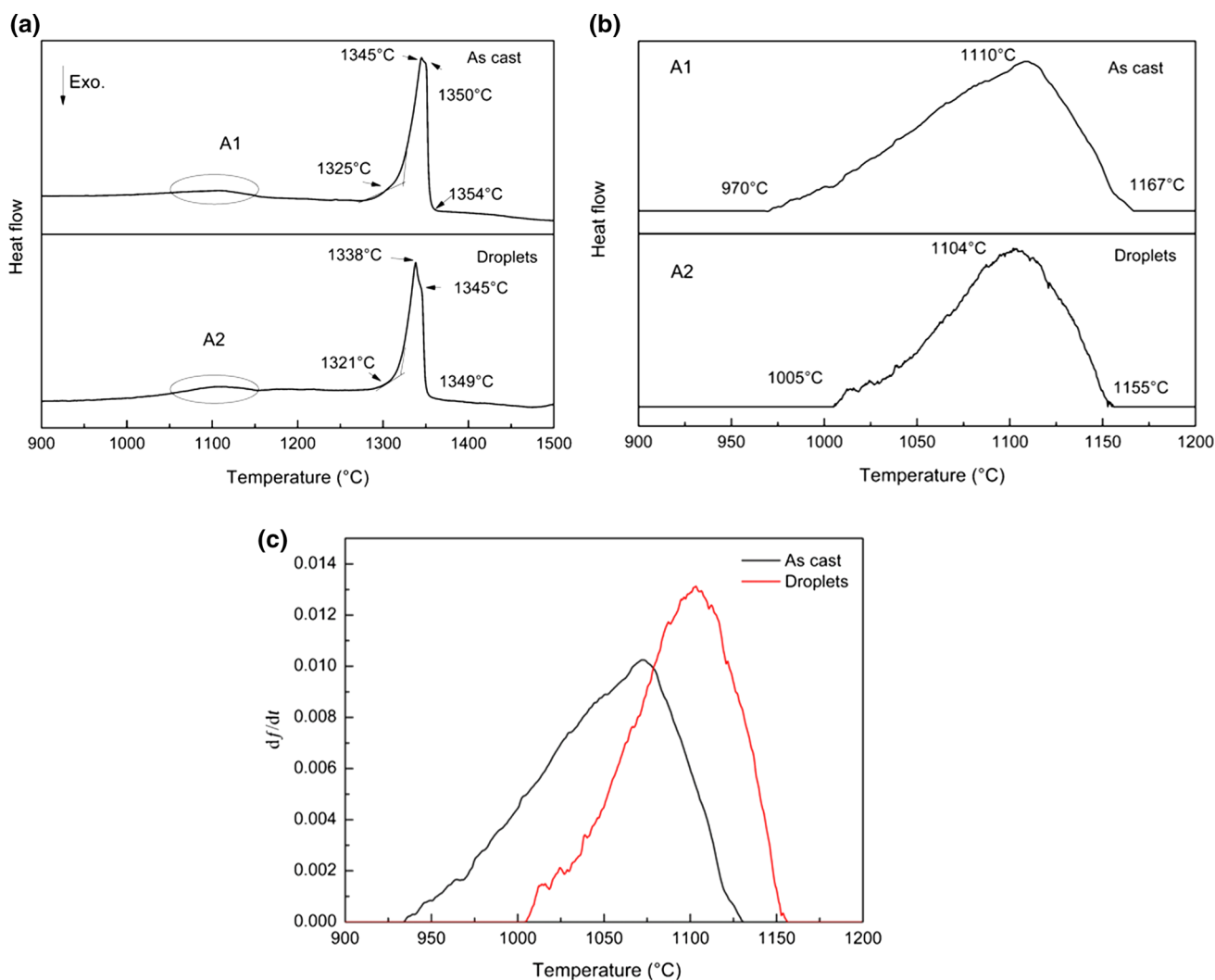


**Fig. 8** **a** DSC heating curves obtained from as-cast alloy and droplet sample ( $D = 1000 \mu\text{m}$ ,  $R_c = 5.2 \times 10^2 \text{ K s}^{-1}$ ), **b** enlarged areas A1, A2 in Fig. 8a, **c**  $\gamma'$  precipitation rate ( $df/dt$ ) as function of temperature ( $T$ )

observed: large cuboidal  $\gamma'_{\text{I}}$  and nano-quasi-spherical  $\gamma'_{\text{II}}$  precipitates within the  $\gamma$  phase. This situation is shown in Fig. 1b.

In the case of droplets cooled at high cooling rates, most of the transformation occurs at low temperatures where nucleation is high. This condition promotes high nucleation burst of  $\gamma'$  precipitates and rapid transformation. Simultaneously with the nucleation of precipitates, the formed  $\gamma'$  precipitates grow by diffusional transport of atoms. Depending on the mobility of the atoms and the time available for diffusion as a function of cooling rate, each precipitate can be assigned to a characteristic diffusion field, which denotes the region where solute atoms can be gathered [26, 27]. There is insufficient time for those  $\gamma'$  precipitates to aggregate and merge. As a result, only nano- $\gamma'$  precipitates exist in the microstructure without large cuboidal  $\gamma'$  (Figs. 6 and 7). The  $\gamma'$  precipitates are more inclined to present spherical without inconspicuous

crystallographic features (parallel to the cube directions in the  $\langle 001 \rangle$  directions).

Moreover, in order to analyze the stability and process of  $\gamma'$  precipitate dissolution, the DSC heating curves obtained from droplet sample ( $D = 1000 \mu\text{m}$ ,  $R_c = 5.2 \times 10^2 \text{ K s}^{-1}$ ) and as-cast alloy are provided (Fig. 8a), respectively. For both as-cast alloy and droplet sample, the latter two endothermic peaks are corresponding to the melting of  $\gamma' + \gamma$  eutectic and the  $\gamma$  phase, respectively. The first endothermic peak represents the dissolution of  $\gamma'$  precipitate into  $\gamma$  phase. And the area of first endothermic peak (Fig. 8a) is enlarged and shown in Fig. 8b. It can be seen that the initiative dissolving temperature of  $\gamma'$  in as-cast sample is 970 °C which is lower than that in the droplet sample (1005 °C). The reason is that nano-quasi-spherical  $\gamma'_{\text{II}}$  precipitates with high surface energy tend to dissolve into  $\gamma$  phase at relatively low temperature. However, the complete dissolution of large

cuboidal  $\gamma'_I$  precipitates needs to be at high temperature (1167 °C), compared to  $\gamma'$  precipitates (30–50 nm) in droplet sample (1155 °C).

The  $\gamma'$ -phase fraction ( $f$ ) was calculated from the recorded relative heat flow changes  $\Delta H/\Delta H_{\text{tot}}$  (with  $\Delta H_{\text{tot}}$  as the total exothermic heat of the  $\gamma'$ -phase precipitation and  $\Delta H$  as the exothermic heat during the isochronal  $\gamma'$ -phase precipitation) applying the rule as described in Refs. [28, 29]. The thus obtained  $\gamma'$  precipitation rate ( $df/dt$ ) is presented as function of temperature ( $T$ ) in Fig. 8c. The precipitation rates of  $\gamma'$  phase are quite slow, the maximum values of which are less than 0.014 (Fig. 8c), and the sluggish dissolution process results from the slow diffusion rates of atoms. Meanwhile, it is noted that the exact process and dynamics of dissolution of  $\gamma'$  phase remain to be analyzed and explored in further research.

## 4 Conclusion

A series of droplets with varying diameters (cooling rates) was obtained, and the effect of cooling rate on the microstructure and phase transformation of Ni<sub>3</sub>Al-based superalloy was studied. The cooling rate ( $R_c$ ) is a function of diameter ( $D$ ) of droplets. With the decrease in droplet size ( $D$ ), the cooling rate ( $R_c$ ) increases sharply. The volume fraction of  $\gamma' + \gamma$  eutectic structure increases from 21.31% ( $D = 1400 \mu\text{m}$ ,  $R_c = 3.6 \times 10^2 \text{ K s}^{-1}$ ) to 36.31% ( $D = 270 \mu\text{m}$ ,  $R_c = 2.3 \times 10^3 \text{ K s}^{-1}$ ). In dendritic cores, the feature of  $\gamma'$  precipitate is also obviously changed with increasing cooling rate. The bimodal size distributions of  $\gamma'$  precipitates disappear, which is normal in as-cast alloys. Instead, a lot of nano- $\gamma'$  precipitates exist in the droplets due to high nucleation burst.

**Acknowledgements** This work was supported by the National Natural Science Foundation of China (Nos. 51774212 and 51674175).

## References

- [1] A.R.P. Singh, S. Nag, J.Y. Hwang, G.B. Viswanathan, J. Tiley, R. Srinivasan, H.L. Fraser, R. Banerjee, *Mater. Charact.* **62**, 878 (2011)

- [2] Y.C. Liu, Q.Y. Guo, C. Li, Y.P. Mei, X.S. Zhou, Y. Huang, H.J. Li, *Acta Metall. Sin.* **52**, 1259 (2016). (in Chinese)
- [3] Z.X. Shi, S.Z. Liu, X.G. Wang, J.R. Li, *Acta Metall. Sin. (Engl. Lett.)* **30**, 614 (2017)
- [4] T.M. Smith, B.D. Esser, N. Antolin, A. Carlsson, R.E.A. Williams, A. Wessman, T. Hanlon, H.L. Fraser, W. Windl, D.W. McComb, M.J. Mills, *Nat. Commun.* **7**, 13434 (2016)
- [5] H.P. Wang, C.H. Zheng, P.F. Zou, S.J. Yang, L. Hu, B. Wei, *J. Mater. Sci. Technol.* **34**, 436 (2018)
- [6] G. Li, B. Chen, Z.H. Du, L. Zhang, Y.C. Ma, K. Liu, *J. Mater. Sci. Technol.* **34**, 811 (2018)
- [7] L.Q. Cui, J.J. Yu, J.L. Liu, J. Tao, X.F. Sun, *Mater. Sci. Eng., A* **710**, 309 (2018)
- [8] Y.B. Hu, L. Zhang, C.Q. Zhang, P.T. Zhao, G.P. Guo, J. Zhao, *Acta Metall. Sin. (Engl. Lett.)* **30**, 857 (2017)
- [9] Y. Zhang, Q. Wang, H.G. Dong, C. Dong, H.Y. Zhang, X.F. Sun, *Acta Metall. Sin. (Engl. Lett.)* **31**, 127 (2018)
- [10] C.T. Liu, V.K. Sikka, *JOM* **38**, 19 (1986)
- [11] V.K. Sikka, S.C. Deevi, S. Viswanathan, R.W. Swindeman, M.L. Santella, *Intermetallics* **8**, 1329 (2000)
- [12] J. Ding, S. Jiang, Y.T. Wu, Y.M. Li, X.C. Xia, C. Li, Y.C. Liu, *Mater. Lett.* **211**, 5 (2018)
- [13] G. Li, B. Chen, Z.H. Du, M.S. Zhang, R.C. Liu, K. Liu, *J. Mater. Sci. Technol.* **34**, 541 (2018)
- [14] Z.D. Fan, D. Wang, C. Liu, G. Zhang, J. Shen, L.H. Lou, J. Zhang, *Acta Metall. Sin. (Engl. Lett.)* **30**, 878 (2017)
- [15] G. Liu, L. Liu, C. Ai, B.M. Ge, J. Zhang, H.Z. Fu, *J. Alloys Compd.* **509**, 5866 (2011)
- [16] C. Ai, S.S. Li, H. Zhang, L. Liu, Y. Ma, Y.L. Pei, S.K. Gong, *J. Alloys Compd.* **592**, 164 (2014)
- [17] B.C. Wilson, E.R. Cutler, G.E. Fuchs, *Mater. Sci. Eng., A* **479**, 356 (2008)
- [18] S. Milenkovic, I. Sabirov, J. Llorca, *Mater. Lett.* **73**, 216 (2012)
- [19] Y.J. Zhang, Y.J. Huang, L. Yang, J.G. Li, *J. Alloys Compd.* **570**, 70 (2013)
- [20] C.D. Cao, W.J. Xie, B. Wei, *Mater. Sci. Eng., A* **344**, 10 (2003)
- [21] J.Q. Yu, *Atlas of Binary Alloys Phase Diagram* (Shanghai Scientific and Technical Publishers, Shanghai, 1983)
- [22] J. Wu, Y.C. Liu, C. Li, X.C. Xia, Y.T. Wu, H.J. Li, H.P. Wang, *Acta Metall. Sin. (Engl. Lett.)* **30**, 949 (2017)
- [23] C.G. Levi, R. Mehrabian, *Metall. Trans. A* **13**, 221 (1982)
- [24] K. Wu (ed.), *Transport Principles of Metallurgical Processes* (Metallurgical Industry Press, Beijing, 2011)
- [25] R. Radis, M. Schaffer, M. Albu, G. Kothleitner, P. Polt, E. Kozeschnik, *Acta Mater.* **57**, 5739 (2009)
- [26] Y.H. Wen, J.P. Simmons, C. Shen, C. Woodward, Y. Wang, *Acta Mater.* **51**, 112 (2003)
- [27] J. Kundin, L. Mushongera, T. Goehler, H. Emmerich, *Acta Mater.* **60**, 3758 (2012)
- [28] J. Coakley, H. Basoalto, D. Dye, *Acta Mater.* **58**, 4019 (2010)
- [29] S.S. Hosseini, S. Nategh, A.A. Ekrami, *J. Alloys Compd.* **512**, 340 (2012)